INTERNATIONAL JOURNAL FOR NUMERICAL METHODS IN ENGINEERING
Int. J. Numer. Meth. Engng 2013; **93**:224–244
Published online 5 July 2012 in Wiley Online Library (wileyonlinelibrary.com). DOI: 10.1002/nme.4393

An embedded formulation with conforming finite elements to capture strong discontinuities

D. Dias-da-Costa[1,3,*,†], J. Alfaiate[2,4], L. J. Sluys[5], P. Areias[2,6] and E. Júlio[2,4]

[1]*INESC Coimbra, Rua Antero de Quental 199, 3000-033 Coimbra, Portugal*
[2]*ICIST, 1049–001 Lisboa, Portugal*
[3]*Civil Eng. Dept., University of Coimbra, Rua Luís Reis Santos, 3030–788 Coimbra, Portugal*
[4]*Civil Eng. Dept., Instituto Superior Técnico, Av. Rovisco Pais, 1049–001 Lisboa, Portugal*
[5]*Dept. of Civil Engineering and Geosciences, Delft University of Technology, P.O. Box 5048, 2600 GA Delft, The Netherlands*
[6]*Physics Dept., University of Évora, Colégio Luís António Verney, Rua Romão Ramalho 59, 7002–554 Évora, Portugal*

SUMMARY

The embedding of discontinuities into finite elements has become a powerful technique for the simulation of fracture in a wide variety of mechanical problems. However, existing formulations still use non-conforming finite elements. In this manuscript, a new conforming formulation is proposed. The main properties of this formulation are as follows: (i) variational consistency; (ii) no limitations on the choice of the parent finite element; (iii) comprehensive kinematics of the discontinuity, including both rigid body motion and stretching; (iv) fully compatible enhanced kinematic field; (v) additional global DOFs located at the discontinuity; (vi) continuity of both jumps and tractions across element boundaries; and (vii) *stress locking* free. The performance of the proposed formulation is tested by means of academic and structural examples. The numerical results are compared with available experimental results and other numerical approaches, namely the generalized strong discontinuity approach and the generalized FEM/Extended FEM. Copyright © 2012 John Wiley & Sons, Ltd.

Received 7 November 2011; Revised 26 April 2012; Accepted 17 June 2012

KEY WORDS: strong embedded discontinuity; discrete cracking; conforming elements; non-homogeneous jumps

NOMENCLATURE

$\mathbf{a}$	total displacement vector at the nodes
$\hat{\mathbf{a}}$	regular displacement vector at the nodes
$\tilde{\mathbf{a}}$	enhanced displacement vector at the nodes
$\bar{\mathbf{b}}$	body forces vector
$\mathbf{B}$	strain-nodal displacement matrix
$\mathbf{B}_w$	enhanced strain-nodal displacement matrix
c_0	cohesion
$\mathbf{D}$	constitutive matrix
E	Young's modulus
$\hat{\mathbf{f}}$	vector force at the regular nodes
f_c	compressive strength
f_t	tensile strength

*Correspondence to: D. Dias-da-Costa, INESCC, Civil Engineering Department, University of Coimbra, Rua Luís Reis Santos, 3030–788 Coimbra, Portugal.

†E-mail: dias-da-costa@dec.uc.pt

$\mathbf{f}_w$	vector force at the additional nodes
G_F	fracture energy
h	parameter defining the jump transmission to Ω^+ and Ω^-
H_{Γ_d}	function measuring the jump transmission to Ω^+ and Ω^-
$\mathbf{H}_{\Gamma_d}$	diagonal matrix containing the Heaviside function evaluated at each DOF
$\mathcal{H}_{\Gamma_d}$	Heaviside function
i, j	nodes placed at both extremities of the discontinuity
$\mathbf{I}$	identity matrix
k_n, k_s	normal and shear penalty parameters, respectively
$\mathbf{K}_{aa}$	bulk stiffness matrix
$\mathbf{K}_{aw}, \mathbf{K}_{wa}, \mathbf{K}_{ww}$	enhanced bulk stiffness matrices
$\mathbf{K}_d$	discontinuity stiffness matrix
l	measure of distance around the tip
l_{ch}	Hillerborg's characteristic length
l_d	discontinuity length
$\mathbf{L}$	differential operator matrix
$\mathbf{M}_{\mathbf{R_w}}$	matrix transmitting the rigid body motion from the discontinuity opening
$\mathbf{M}_{\mathbf{nR_w}}$	matrix transmitting the non–rigid body motion from the discontinuity opening
$\mathbf{M}_w$	matrix transmitting the displacement resulting from the discontinuity opening
$\mathbf{M}_w^{k^*}$	matrix containing the contribution of the discontinuities of all enriched elements to each node of the element
n	number of finite element nodes
$\mathbf{n}$	unit vector normal to the boundary
$\mathbf{n}^+$	unit vector normal to the discontinuity surface
n_{el}	number of enriched elements
$\mathbf{N}$	shape function matrix
$\mathbf{N}_w$	enhanced shape function matrix
$\mathbf{m}$	unit vector with the direction of the jump
P	external load
r	distance between the integration point and the discontinuity tip
$\mathbf{s}$	unit vector tangent to the discontinuity
$\mathbf{t}$	traction vector
$\bar{\mathbf{t}}$	natural forces vector
$\mathbf{T}$	discontinuity constitutive matrix
$\mathbf{u}$	total displacement vector
$\bar{\mathbf{u}}$	essential boundary conditions vector
$\hat{\mathbf{u}}$	regular displacement field vector
$\tilde{\mathbf{u}}$	enhanced displacement field vector
$[\![\mathbf{u}]\!]$	jump vector
u_v	vertical displacement
$\mathbf{w}^*$	nodal jump vector
w_i	weight for the integration point i
$\mathbf{x}$	global coordinates of a material point
$\mathbf{x}_1, \mathbf{x}_2$	global frame
α	discontinuity angle
β	shear contribution parameter
$\boldsymbol{\beta}$	diagonal matrix of the contribution of each enriched element
Γ	boundary
Γ_d	discontinuity surface
Γ_t	boundary with natural forces
Γ_u	boundary with essential conditions
$\boldsymbol{\varepsilon}$	total strain tensor
$\boldsymbol{\sigma}$	stress tensor

DOI: 10.1002/nme

σ_1	first principle stress
ν	Poisson's ratio
Ω	body
$d(\cdot)$	incremental variation of $(\cdot)$
$(\cdot)^s$	symmetric part of $(\cdot)$
$\delta(\cdot)$	admissible or virtual variation of $(\cdot)$
δ_{Γ_d}	Dirac's delta-function along the surface Γ_d
$(\cdot)^e$	$(\cdot)$ belonging to the finite element e
$(\cdot)^+$, $(\cdot)^-$	$(\cdot)$ at the positive and negative side of the discontinuity, respectively
$(\cdot)_n$, $(\cdot)_s$	normal and shear component of $(\cdot)$

1. INTRODUCTION

The embedding of discontinuities into finite elements is a powerful technique for the simulation of fracture in a wide variety of mechanical problems, namely brickwork masonry fracture [1, 2], dynamic fracture [3], failure in finite strain problems [4, 5], and simulation of reinforced concrete members [6, 7].

The first formulations were developed within the enhanced assumed strain method framework (EAS) [8]. Typically, constant jumps are embedded using constant strain triangles (CST), and full advantage of the static condensation of additional DOFs is adopted [9–16]. However, with these formulations: (i) no inter-element continuity requirement is imposed on the enhanced strain field; and, as a consequence, (ii) no traction continuity across element boundaries is obtained.

Bolzon [17] presented an innovative formulation with conforming elements to capture the rigid body opening of the discontinuity. For that purpose the additional DOFs are: (i) placed at the edges of the enriched element; and (ii) defined at global level to enforce traction continuity across elements. The major drawback remains the fact that only CST elements can be adopted. Moreover, only very simple structural examples have been presented.

Alfaiate *et al.* [18] introduced an approach for embedding interface elements into *any* parent element, capturing linear jumps along the discontinuity. This formulation was developed within the framework of the discrete crack approach. A discussion concerning the advantages of using local (static condensation) or global additional DOFs was also presented by the authors. The latter option was adopted to ensure traction continuity across element edges. Dias-da-Costa *et al.* [19] provided a variationally consistent formulation handling rigid body jump transmission induced by the opening of the discontinuity. It was proved that this formulation satisfies Simo's orthogonality condition [9] exactly. Consequently, the enhanced displacement field induces a null strain field, and the discontinuity behaviour is decoupled from the bulk behaviour. Additionally, the modelling of the discontinuity is performed as an internal interface of the element.

Linder and Armero [20] developed a general framework to embed both rigid and stretching opening modes of the discontinuity into *any* parent element. Because the authors took advantage of static condensation, traction continuity is not obtained. A variationally consistent formulation with traction continuity was introduced by Dias-da-Costa *et al.* [21], called the generalized strong discontinuity approach (GSDA). The GSDA considers the rigid body motion and stretching of Ω^+ over Ω^-, the domains at both sides of the discontinuity. However, although jumps and tractions remain continuous across element boundaries, no inter-element continuity of the enhanced displacement field is achieved in the GSDA.

Despite the earlier mentioned relevant contributions to this field, a general embedded formulation capable of dealing with strong discontinuities using conforming finite elements is still missing. Figures 1(a)–(c) are used to illustrate what occurs with a typical deformed mesh where displacements are magnified 200 times:

- in Figure 1(a) the usual representation is shown, where only the regular nodes of each element are represented. Therefore, the enriched elements remain unpartitioned and seem compatible, although distorted;

DOI: 10.1002/nme

- Figure 1(b) corresponds to Figure 1(a), but now, each enriched element has the discontinuity truly represented inside the parent element and the corresponding domain becomes partitioned. Therefore, the non-conformity of the elements becomes evident;
- in Figure 1(c), the expected deformed mesh obtained with a fully conforming formulation is shown.

It is important to emphasise that although the additional DOFs may be global [18, 19, 21], non-conformity still appears, although less significant, between enriched elements and at the tip of the crack (Figure 2).

2. RESEARCH SIGNIFICANCE

A new general *conforming* embedded formulation is proposed here, aiming to fulfil the following main objectives: (i) variational consistency; (ii) comprehensive kinematics of the discontinuity including both rigid body motion and stretching; (iii) no limitation on the choice of the parent finite element; (iv) additional DOFs located at the discontinuity; (v) continuity of both jumps and tractions across element boundaries by using global additional DOFs; (vi) fully compatible displacement field; and (vii) *stress locking* free.

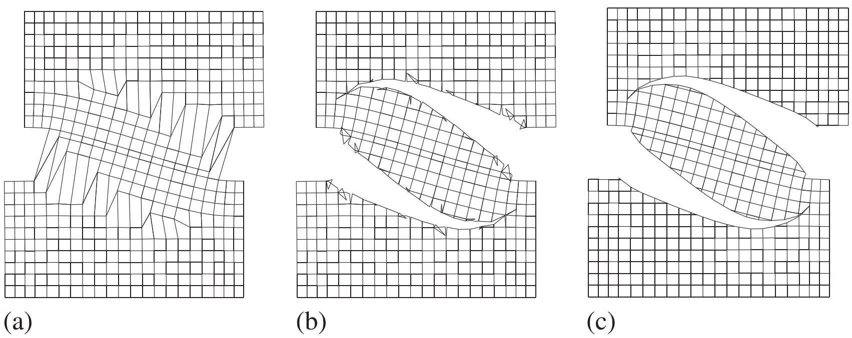

Figure 1. Deformed mesh obtained using embedded elements (displacements magnified 200 times): (a) classic representation of (apparently compatible) deformed elements; (b) representation of the true deformed mesh revealing non-conforming elements; and (c) solution with conforming elements.

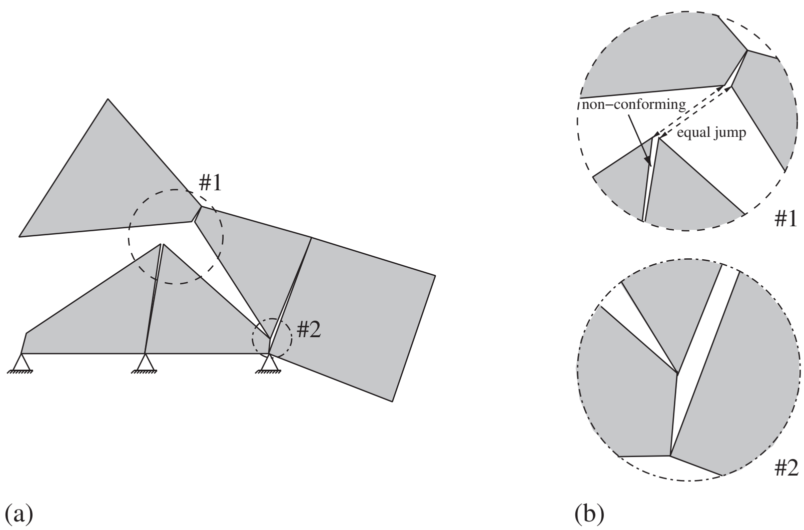

Figure 2. Traction continuity: (a) identification of non-conformity of the elements; and (b) details #1 and #2 showing, respectively, non-conformity between enriched elements and at the tip of the crack.

The manuscript is organised in the following main sections. The general framework is briefly reviewed in Section 3, including the kinematics of a strong discontinuity and the variational principle. Afterwards, the element technology issues are discussed in Section 4. The most relevant results, obtained from both academic and structural examples, are presented and discussed in Section 5. The presented examples have been chosen to illustrate the capabilities of the proposed formulation by comparison to both experimental results and results obtained with other relevant formulations, namely the GSDA [21] and generalized/extended FEM (GFEM/XFEM) [22–25].

3. GENERAL FRAMEWORK

3.1. Kinematics of a strong discontinuity

Consider a body Ω with an external boundary Γ and an internal boundary, which is the discontinuity Γ_d, dividing the domain in two subregions: Ω^+ and Ω^- (Figure 3).

A quasi-static loading of body forces $\bar{\mathbf{b}}$ and natural boundary conditions $\bar{\mathbf{t}}$, distributed on the external boundary Γ_t, is applied to the body. The essential boundary conditions $\bar{\mathbf{u}}$ are prescribed at boundary Γ_u, such that: $\Gamma_t \cup \Gamma_u = \Gamma$ and $\Gamma_t \cap \Gamma_u = \varnothing$. The Vector $\mathbf{n}$ is orthogonal to the boundary surface, pointing outwards, whilst $\mathbf{n}^+$ is orthogonal to the discontinuity and pointing inwards Ω^+.

Distinct approaches can be considered regarding the way the jump is transmitted by the discontinuity to the domain Ω. The most general one considers the independent enhanced displacement field composed by $\tilde{\mathbf{u}}^+$ and $\tilde{\mathbf{u}}^-$ on Ω^+ and Ω^-, respectively [17, 26]. However, the direct consequence of this procedure is the duplication of the number of DOFs at the discontinuity. A possible simplification consists of assuming a constant scalar factor, $0 \leqslant h \leqslant 1$, partitioning the jump [13, 18, 27–29] (Figure 3). Accordingly, the total displacement $\mathbf{u}$ is composed by the sum of two parts: (i) the regular displacement field $\hat{\mathbf{u}}$; and (ii) the enhanced displacement field $\tilde{\mathbf{u}}$, induced by the jumps at the discontinuity:

$$\mathbf{u}(\mathbf{x}) = \hat{\mathbf{u}}(\mathbf{x}) + H_{\Gamma_d}\tilde{\mathbf{u}}(\mathbf{x}), \tag{1}$$

where H_{Γ_d} is the function establishing the way the jump is transmitted by the discontinuity:

$$H_{\Gamma_d} = \mathcal{H}_{\Gamma_d} - (1-h), \quad 0 \leqslant h \leqslant 1, \tag{2}$$

with $\mathcal{H}_{\Gamma_d}$ denoting the standard Heaviside function:

$$\mathcal{H}_{\Gamma_d} = \begin{cases} 1 & \text{in } \Omega^+ \\ 0 & \text{otherwise} \end{cases}. \tag{3}$$

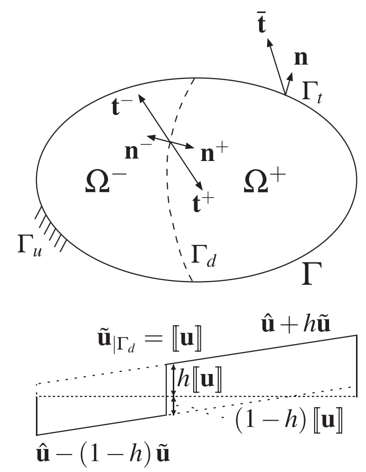

Figure 3. Domain Ω crossed by a strong discontinuity Γ_d and one-dimensional representation of displacement and strain fields.

DOI: 10.1002/nme

The jump at the discontinuity is obtained by evaluating the enhanced displacement field along the discontinuity according to

$$[\![\mathbf{u}]\!] = (\mathbf{u}^+ - \mathbf{u}^-)_{|\Gamma_d} = \tilde{\mathbf{u}}_{|\Gamma_d}. \tag{4}$$

The jump $[\![\mathbf{u}]\!]$ can be expressed in the following form:

$$[\![\mathbf{u}]\!] = [\![u]\!]\mathbf{m}, \tag{5}$$

with $[\![u]\!]$ and $\mathbf{m}$ representing the modulus and direction of the jump, respectively. When $\mathbf{m}$ is parallel to $\mathbf{n}^+$, the crack opens in pure mode-I; if $\mathbf{m}$ is parallel to the crack, mode-II failure is obtained.

For small displacements, the strain field is

$$\boldsymbol{\varepsilon} = \nabla^{\mathrm{s}}\mathbf{u} = \underbrace{\nabla^{\mathrm{s}}\hat{\mathbf{u}} + H_{\Gamma_d}\left(\nabla^{\mathrm{s}}\tilde{\mathbf{u}}\right)}_{\text{bounded}} + \underbrace{\delta_{\Gamma_d}\left([\![\mathbf{u}]\!] \otimes \mathbf{n}^+\right)^{\mathrm{s}}}_{\text{unbounded}} \quad \text{in } \Omega, \tag{6}$$

where $(\cdot)^s$ is the symmetric part of $(\cdot)$ and $\otimes$ is the dyadic product. It is highlighted that the unbounded term in Equation (6) vanishes outside Γ_d.

For most situations, the solution is independent of h due to the enforcement of both essential and natural boundary conditions [26]. Therefore, it is hereafter assumed that $h = 1$ which, according to Equation (2), leads to $H_{\Gamma_d} = \mathcal{H}_{\Gamma_d}$, being the jump entirely transmitted from Ω^- to Ω^+.

3.2. *Variational formulation*

The following equation states the principle of virtual work for a continuum media with a discontinuity:

$$-\int_{\Omega\backslash\Gamma_d} \left(\nabla^{\mathrm{s}}\delta\mathbf{u}\right) : \boldsymbol{\sigma}\left(\boldsymbol{\varepsilon}\right) \mathrm{d}\Omega - \int_{\Gamma_d} \delta[\![\mathbf{u}]\!] \cdot \mathbf{t}^+ \mathrm{d}\Gamma + \int_{\Omega\backslash\Gamma_d} \delta\mathbf{u} \cdot \bar{\mathbf{b}} \mathrm{d}\Omega + \int_{\Gamma_t} \delta\mathbf{u} \cdot \bar{\mathbf{t}} \mathrm{d}\Gamma = 0. \tag{7}$$

where (i) the first integral is the internal work; and (ii) the third and fourth terms are the external work. Both (i) and (ii) are the usual terms adopted in a continuum approach. The second term is the work produced at the discontinuity.

It is stressed that the variational formulation represented by Equation (7) was already obtained by Malvern [30] by progressively applying the principle of virtual work to each subregion Ω^+ and Ω^- (Figure 3), where the discontinuity is taken as an external boundary.

4. ELEMENT TECHNOLOGY

In this section, the general framework for obtaining conforming enriched elements, namely the jump transmission technique, the discretised equations and the crack propagation issues are presented.

4.1. *Element interpolation*

Consider a finite element partition of the two-dimensional domain Ω. Each finite element Ω^e, with n nodes, crossed by a straight discontinuity Γ_d^e, is divided in two subdomains. The adopted conventions are represented in Figure 4(a).

The following equation provides the approximation of the displacement field for each enriched finite element with n nodes:

$$\mathbf{u}^e = \mathbf{N}^e(\mathbf{x})\left(\hat{\mathbf{a}}^e + \mathcal{H}_{\Gamma_d}\tilde{\mathbf{a}}^e\right) \quad \text{if } \mathbf{x} \in \Omega^e \setminus \Gamma_d^e, \tag{8}$$

where $\mathbf{N}^e$ contains the element shape functions, $\hat{\mathbf{a}}^e$ are the nodal DOFs related to $\hat{\mathbf{u}}^e$ and $\tilde{\mathbf{a}}^e$ are the enhanced nodal DOFs related to $\tilde{\mathbf{u}}^e$.

The previous equation can be rearranged by noticing that $\hat{\mathbf{a}}^e$ is given by

$$\hat{\mathbf{a}}^e = \mathbf{a}^e - \mathbf{H}^e_{\Gamma_d}\tilde{\mathbf{a}}^e, \tag{9}$$

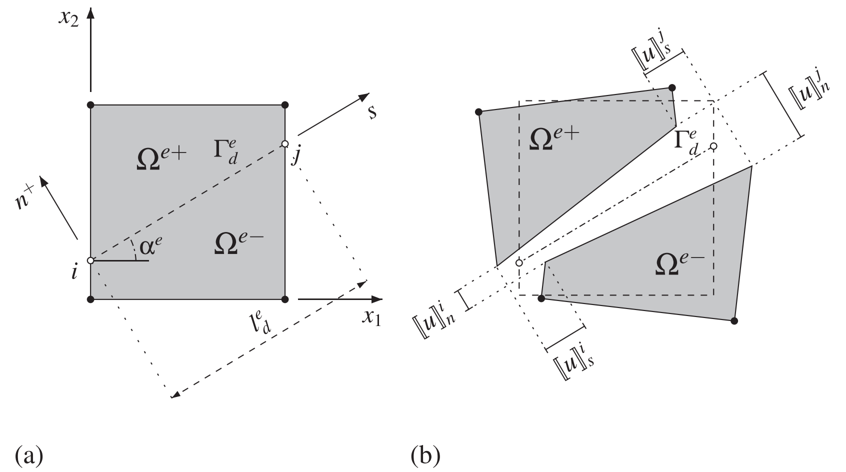

Figure 4. Domain Ω^e crossed by a strong discontinuity Γ_d^e: (a) definitions; and (b) general opening.

with $\mathbf{a}^e$ being the total nodal DOFs related to $\mathbf{u}^e$, $\mathbf{H}^e_{\Gamma_d}$ is a $(2n \times 2n)$ diagonal matrix with components equal to '1' for nodal DOFs in Ω^{e+} and components equal to '0', otherwise.

Replacing Equation (9) into Equation (8), the following can be conveniently written:

$$\mathbf{u}^e = \mathbf{N}^e(\mathbf{x})\left[\mathbf{a}^e + \left(\mathcal{H}_{\Gamma_d}\mathbf{I} - \mathbf{H}^e_{\Gamma_d}\right)\tilde{\mathbf{a}}^e\right] \quad \text{if } \mathbf{x} \in \Omega^e \setminus \Gamma_d^e. \tag{10}$$

The jump at the discontinuity can be obtained using Equation (10) applied at both sides of the discontinuity:

$$[\![\mathbf{u}]\!]^e = \mathbf{u}^{e+} - \mathbf{u}^{e-} = \mathbf{N}^e(\mathbf{x})\tilde{\mathbf{a}}^e \quad \text{at } \Gamma_d^e. \tag{11}$$

To capture the kinematics of the discontinuity regarding both rigid body motion and stretching of Ω^+ over Ω^-, two additional nodes are placed at the edges of each enriched element [18, 19, 21, 31] (Figure 4(b)). Therefore, the enhanced nodal DOFs become

$$\tilde{\mathbf{a}}^e = \mathbf{M}_w^{ek^*}\mathbf{w}^{e^*}, \tag{12}$$

where $\mathbf{w}^{e^*}$ is a vector formed by juxtaposing by rows the additional DOFs resulting from the contribution of the following n_{el} enriched elements: (i) element e; and (ii) all remaining enriched elements sharing at least one node with element e. Matrix $\mathbf{M}_w^{ek^*}$ has also the contribution of all these enriched elements, such that each row, $\mathbf{M}_w^{ei^*}$ is in direct correspondence to the i-node of the element e and can be computed by

$$\mathbf{M}_w^{ei^*} = \mathbf{M}_w^e + \sum_{j=1, j\neq e}^{n_{el}} \left\{\mathbf{M}_w^j - \mathbf{M}_w^e\right\}\boldsymbol{\beta}^j, \tag{13}$$

where $\mathbf{M}_w^e$ is responsible for transmitting the jumps to the element nodes and can be decomposed into

$$\mathbf{M}_w^e = \mathbf{M}_{R_w}^e + \mathbf{M}_{nR_w}^e, \tag{14}$$

with

$$\mathbf{M}_{R_w}^e = \begin{bmatrix} 1 - \frac{\left(x_2 - x_2^i\right)\sin\alpha^e}{l_d^e} & \frac{\left(x_2 - x_2^i\right)\cos\alpha^e}{l_d^e} & \frac{\left(x_2 - x_2^i\right)\sin\alpha^e}{l_d^e} & -\frac{\left(x_2 - x_2^i\right)\cos\alpha^e}{l_d^e} \\ \frac{\left(x_1 - x_1^i\right)\sin\alpha^e}{l_d^e} & 1 - \frac{\left(x_1 - x_1^i\right)\cos\alpha^e}{l_d^e} & -\frac{\left(x_1 - x_1^i\right)\sin\alpha^e}{l_d^e} & \frac{\left(x_1 - x_1^i\right)\cos\alpha^e}{l_d^e} \end{bmatrix}, \tag{15}$$

DOI: 10.1002/nme

$$\mathbf{M}^e_{nR_w} = \begin{bmatrix} -\frac{s^e_n(1+\cos(2\alpha^e))}{2} & -\frac{s^e_n(\sin(2\alpha^e))}{2} & \frac{s^e_n(1+\cos(2\alpha^e))}{2} & \frac{s^e_n(\sin(2\alpha^e))}{2} \\ -\frac{s^e_n(\sin(2\alpha^e))}{2} & -\frac{s^e_n(1-\cos(2\alpha^e))}{2} & \frac{s^e_n(\sin(2\alpha^e))}{2} & \frac{s^e_n(1-\cos(2\alpha^e))}{2} \end{bmatrix} \tag{16}$$

and

$$s^e_n = \frac{s\,(\mathbf{x}_i)}{l^e_d} = \left(x_1 - x^i_1\right)\frac{\cos(\alpha^e)}{l^e_d} + \left(x_2 - x^i_2\right)\frac{\sin(\alpha^e)}{l^e_d}, \tag{17}$$

where $\mathbf{x} = (x_1, x_2)$ is the global position of any material point inside the finite element, $\mathbf{x}^i = \left(x^i_1, x^i_2\right)$ is the global position of the tip i (Figure 4(a)), l^e_d is the length of the discontinuity Γ^e_d measured along the local frame $\vec{s}$, and α^e is the discontinuity angle defined in Figure 4(a).

It is stressed that $\mathbf{M}^e_{R_w}$ is the rigid-body part, which includes both normal and constant shear jump components, and $\mathbf{M}^e_{nR_w}$ is the non-rigid stretching part along the discontinuity Γ^e_d (see [21] for more details).

$\boldsymbol{\beta}^j$ is a diagonal matrix computed at each node i, containing $\beta^j_{x_i}$ terms for both directions (x_1, x_2), representing a measure of the relative stiffness contribution of each enriched element for the enhanced displacement field:

$$\beta^j_{x_i} = \frac{K^j_{i,x_i}}{\sum_{k=1}^{n_{el}} K^k_{i,x_i}}, \tag{18}$$

where K^j_{i,x_i} is the stiffness matrix component of the bulk for element j for direction x_i (Figure 4(a)). Thus, according to Equations (13)–(18), a mutual dependence between jumps and bulk deformation is built, leading to a full compatible formulation.

Note that the embedded formulation is obtained as if an interface element were embedded in the parent finite element, whereas the GFEM/XFEM can be interpreted as if two element layers were superimposed. This is why, in the embedded formulations, the transmission of the additional DOFs to the standard nodes has to be performed using $\mathbf{M}^e_w$, which is formulated differently for each embedded formulation: in the DSDA [19], the matrix $\mathbf{M}^e_w$ introduces a rigid body motion of Ω^{e+} with respect to Ω^{e-}, in the GSDA [21], this matrix is generalized to further include stretching and in the present conforming formulation this matrix is again redefined to achieve compatibility (Equation (13)). In the GFEM/XFEM, there is no such transmission of the DOFs because they are obtained directly at the standard node locations and not at the discontinuity (a complete comparative study can be found in [32]).

Finally, by inserting Equation (12) into Equations (10) and (11) the interpolation of the total displacement and jump fields becomes

$$\mathbf{u}^e = \mathbf{N}^e(\mathbf{x})\left[\mathbf{a}^e + \left(\mathcal{H}_{\Gamma_d}\mathbf{I} - \mathbf{H}^e_{\Gamma_d}\right)\mathbf{M}^{ek^*}_w \mathbf{w}^{e^*}\right] \quad \text{if } \mathbf{x} \in \Omega^e \setminus \Gamma^e_d, \tag{19a}$$

$$[\![\mathbf{u}]\!]^e = \mathbf{u}^{e+} - \mathbf{u}^{e-} = \mathbf{N}^e(\mathbf{x})\mathbf{M}^{ek^*}_w \mathbf{w}^{e^*} \quad \text{at } \Gamma^e_d. \tag{19b}$$

The discrete version of the strain field is given by

$$\boldsymbol{\varepsilon}^e = \underbrace{\mathbf{L}\mathbf{N}^e(\mathbf{x})}_{\mathbf{B}^e(\mathbf{x})}\left[\mathbf{a}^e + \left(\mathcal{H}_{\Gamma_d}\mathbf{I} - \mathbf{H}^e_{\Gamma_d}\right)\mathbf{M}^{ek^*}_w \mathbf{w}^{e^*}\right] \quad \text{in } \Omega^e \setminus \Gamma^e_d, \tag{20}$$

where $\mathbf{L}$ is the usual differential operator. The incremental stress field is

$$\mathrm{d}\boldsymbol{\sigma}^e = \mathbf{D}^e\mathbf{B}^e\left[\mathrm{d}\mathbf{a}^e + \left(\mathcal{H}_{\Gamma_d}\mathbf{I} - \mathbf{H}^e_{\Gamma_d}\right)\mathbf{M}^{ek^*}_w \mathrm{d}\mathbf{w}^{e^*}\right] \quad \text{in } \Omega^e \setminus \Gamma^e_d, \tag{21}$$

and the traction at the discontinuity, in incremental format, reads:

$$\mathrm{d}\mathbf{t}^e = \mathbf{T}^e \mathrm{d}[\![\mathbf{u}]\!]^e = \mathbf{T}^e\mathbf{N}^e(\mathbf{x})\mathbf{M}^{ek^*}_w \mathrm{d}\mathbf{w}^{e^*} \quad \text{at } \Gamma^e_d, \tag{22}$$

where $\mathbf{D}^e$ and $\mathbf{T}^e$ are, respectively, the bulk and the discontinuity constitutive matrices. The latter constitutive law can be either elastic, for which only the diagonal coefficients are given, or derived from damage theories [25, 31], or plasticity theories [31, 33–36].

4.2. Discretised equations

Equation (7) is discretised using Equations (19a) to (22) and by successively taking: (i) $\delta \mathrm{d}\mathbf{w}^{e^*} = \mathbf{0}$; and (ii) $\delta \mathrm{d}\mathbf{a}^e = \mathbf{0}$, the following system of equations is obtained:

$$\mathbf{K}_{aa}^e \mathrm{d}\mathbf{a}^e + \mathbf{K}_{aw}^e \mathrm{d}\mathbf{w}^{e^*} = \mathrm{d}\hat{\mathbf{f}}^e, \tag{23a}$$

$$\mathbf{K}_{wa}^e \mathrm{d}\mathbf{a}^e + \left(\mathbf{K}_{ww}^e + \mathbf{K}_d^e\right) \mathrm{d}\mathbf{w}^{e^*} = \mathrm{d}\mathbf{f}_w^e, \tag{23b}$$

where:

$$\mathbf{K}_{aa}^e = \int_{\Omega^e \backslash \Gamma_d^e} \mathbf{B}^{e\,T} \mathbf{D}^e \mathbf{B}^e \mathrm{d}\Omega^e, \tag{24}$$

$$\mathbf{K}_{aw}^e = \int_{\Omega^e \backslash \Gamma_d^e} \mathbf{B}^{eT} \mathbf{D}^e \mathbf{B}_w^e \mathrm{d}\Omega^e, \tag{25}$$

$$\mathbf{K}_{wa}^e = \int_{\Omega^e \backslash \Gamma_d^e} \mathbf{B}_w^{eT} \mathbf{D}^e \mathbf{B}^e \mathrm{d}\Omega^e, \tag{26}$$

$$\mathbf{K}_{ww}^e = \int_{\Omega^e \backslash \Gamma_d^e} \mathbf{B}_w^{eT} \mathbf{D}^e \mathbf{B}_w^e \mathrm{d}\Omega^e, \tag{27}$$

$$\mathbf{K}_d^e = \int_{\Gamma_d^e} \mathbf{N}_w^{e\,T} \mathbf{T}^e \mathbf{N}_w^e \mathrm{d}\Gamma^e, \tag{28}$$

with

$$\mathbf{B}_w^e = \mathbf{B}^e \left(\mathcal{H}_{\Gamma_d} \mathbf{I} - \mathbf{H}_{\Gamma_d}^e\right) \mathbf{M}_w^{ek^*} \tag{29}$$

and

$$\mathbf{N}_w^e = \mathbf{N}^e \left(\mathcal{H}_{\Gamma_d} \mathbf{I} - \mathbf{H}_{\Gamma_d}^e\right) \mathbf{M}_w^{ek^*}. \tag{30}$$

The external forces are given by

$$\hat{\mathbf{f}}^e = \int_{\Omega^e \backslash \Gamma_d^e} \mathbf{N}^{e\,T} \bar{\mathbf{b}}^e \mathrm{d}\Omega^e + \int_{\Gamma_t^e} \mathbf{N}^{e\,T} \bar{\mathbf{t}}^e \mathrm{d}\Gamma^e, \tag{31a}$$

$$\mathbf{f}_w^e = \int_{\Omega^e \backslash \Gamma_d^e} \mathbf{N}_w^{eT} \bar{\mathbf{b}}^e \mathrm{d}\Omega^e + \int_{\Gamma_t^e} \mathbf{N}_w^{eT} \bar{\mathbf{t}}^e \mathrm{d}\Gamma^e. \tag{31b}$$

Because traction continuity is enforced in the weak sense, the symmetry of the system of equations is kept if symmetric constitutive matrices are adopted.

4.3. Implementation issues

In this section, the implementation issues concerning crack propagation and path continuity are addressed. Furthermore, the numerical integration of Equations (23a) and (23b) is also briefly explained.

DOI: 10.1002/nme

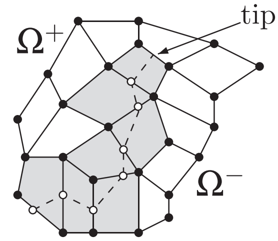

Figure 5. Enriched elements due to crack propagation.

4.3.1. Crack propagation. It is assumed that the discontinuity is straight and crosses an entire parent element and, therefore, the crack tip is always located at the element edge. The finite elements supporting the crack path are enriched (Figure 5), whereas to keep the crack tip closed: (i) no additional DOFs are introduced at this location; (ii) $\mathbf{M}_w^{ei^*}$ is assumed to be zero for nodes supporting the tip. The latter assumption is also traditionally adopted in the GFEM/XFEM [25].

The crack initiation criterion is obtained from a *non-local* stress state adopted near the crack tip, in which case the averaging support is extended beyond the element size [19, 25]. For that, a Gaussian weight function is used to smooth out the stresses at the discontinuity tip:

$$w_i = \frac{1}{(2\pi)^{3/2} l^3} \exp^{\left(-\frac{r^2}{2l^2}\right)}. \tag{32}$$

In Equation (32), w_i is the weight for the integration point i, r is the distance between the integration point and the discontinuity tip, and l is a measure of *significant* distance around the tip. Similarly to [19], l is assumed to be *circa* 1% of Hillerborg's characteristic length [37], given by

$$l_{ch} = \frac{G_F E}{f_{t0}^2}, \tag{33}$$

in which G_F is the fracture energy, f_{t0} is the tensile strength and E is the Young's modulus.

Having obtained the stress at the crack tip, the direction of propagation can be provided by adopting: (i) a function describing a smooth transition between mode-I fracture, mixed-mode and mode-II fracture [19]; or (ii) a Rankine criterion where cracking occurs perpendicularly to the direction of maximum tensile stress. The latter option is herein adopted as it was already shown to provide adequate results for concrete [38].

Traction continuity is enforced in a weak manner, consequently the envelope surface is not reached simultaneously in the bulk and at the discontinuity. At crack initiation, to prevent the traction field at the tip to lie outside the limit surface, a conservative procedure is adopted: the discontinuities are introduced in a slightly earlier stage, in which the stress field in the bulk lies inside the surface ([19]). To avoid convergence difficulties during the iterative procedure, new discontinuities are only inserted at the end of each time step, when updating the internal variables.

4.3.2. Path continuity. The following algorithm, presented in [31], is adopted to enforce continuity of the crack path, which was found to lead to the following: (i) an objective dissipation of energy with respect to the mesh; and (ii) the development of crack patterns similar to those found in experiments, even when reasonably coarse meshes are used. This algorithm does not correspond exactly to a purely local tracking strategy because the stress at the tip is computed by the averaged stress tensor presented in the previous section.

Each time a new discontinuity is inserted, the existence of crack tips in the neighbourhood has to be checked on the element sides:

DOI: 10.1002/nme

1. if no tip is present at the element edges, the crack is enforced to contain the centroid of the element and two new tips are introduced at the adjacent elements;
2. if a tip already exists at the element edge, the new discontinuity is enforced to propagate from that tip;
3. if two tips exist at the element edges, they are connected by inserting a new discontinuity, and the angle is defined by the crack geometry of the problem.

The discontinuity angle remains fixed after crack initiation. Two alternative procedures are available: (i) only one crack is allowed to exist, and each new embedded discontinuity can only be inserted at the crack tip; and (ii) new crack paths are allowed to initiate only outside the neighbourhood of existing crack tips. This neighbourhood is defined by a radius of influence centred at each crack tip with a value of three to five times the maximum aggregate size.

4.3.3. Numerical integration. Equations (25)–(27) require partial integration of Ω^{e+}, the procedure described by [21] is herein adopted. The numerical integration of the discontinuity stiffness matrix given in Equation (28) is performed with a Newton–Cotes/Lobatto scheme to avoid spurious oscillations ([32]).

5. RESULTS

In this section, both element and structural examples of the presented formulation are presented. All examples are computed using bilinear plane stress elements. Both GSDA [21] and GFEM/XFEM [25, 32] are adopted for comparison purposes.

5.1. Element examples

The element examples in this section have been chosen to illustrate the kinematics of the proposed embedded formulation. In Section 5.1.1, two neighbouring elements with different stiffness are enriched, whereas in Section 5.1.2, a small example is used to illustrate the compatibility issues at the tip of a crack front.

5.1.1. Two enriched elements. Consider two enriched elements, each one with dimensions $2 \times 2 \times 1$ mm^3, according to the models represented in Figure 6. In the first model (Figure 6(a)), the left element is softer than the right element, whereas the opposite is assumed for the second model (Figure 6(b)). In both cases, the right discontinuity is stiffer than the left discontinuity.

Linear elastic relationships are adopted for both bulk and discontinuity. The material parameters for the bulk are the following: Young's modulus $E = 10$ N/mm^2 and Poisson's ratio $\nu = 0$ for the softer bulk element; Young's modulus $E = \infty$ and Poisson's ratio $\nu = 0$ for the stiffer bulk element. The discontinuity constitutive matrix (Equation (22)) has the diagonal components related to the normal and shear stiffness equal to: $k_n = k_s = 1$N/mm^3 for the left discontinuity; and $k_n = k_s = \infty$ for the right discontinuity.

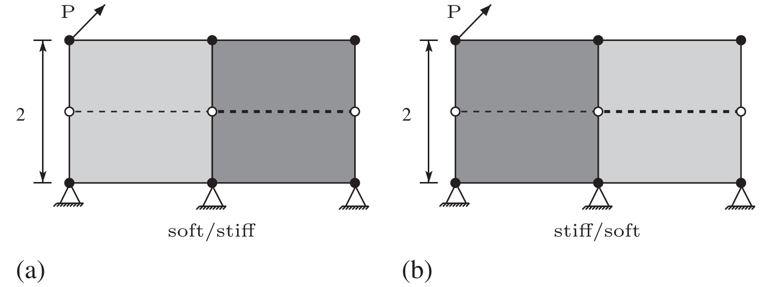

Figure 6. Mesh and loading conditions (dashed line indicates the prescribed discontinuity): (a) first element soft and second element stiff; (b) first element stiff and second element soft.

DOI: 10.1002/nme

The resulting deformed mesh for $P = (1; 1)N$ is represented in Figures 7 and 8 for both cases. It can be concluded that (i) although the GSDA is able to enforce continuous jumps and tractions across elements (see the closed tip between elements in Figures 7(a) and 8(a)), a 'gap' appears between elements due to the non-conforming enrichment; (ii) a conforming enrichment is obtained with the new embedded formulation, which is able to adequately reproduce the kinematics of the discontinuity (similar conclusion regarding GFEM/XFEM); and (iii) less DOFs are required in the new formulation when compared with GFEM/XFEM; consequently, the bulk is discretised with a smaller number of DOFs and this is noticed in particular for the stiff/softer case where the softer element is loaded (compare displacements obtained with both formulations in Figures 7(b) and 8(b)).

5.1.2. Element in front of the tip. The example presented in this section was selected to show the conforming issues appearing due to crack propagation (Figure 2). Three 2×2×1 mm^3 finite elements are considered, where the two elements crossed by a discontinuity are enriched (Figure 9).

Linear elastic properties are considered for both bulk and discontinuity with the following values: Young's modulus $E = 10$ N/mm^2; Poisson's ratio $\nu = 0$; normal and shear stiffness $k_n = k_s =$ 1N/mm^3. The resulting deformed mesh is represented in Figure 10, for $P = (1; 1)N$, from which it

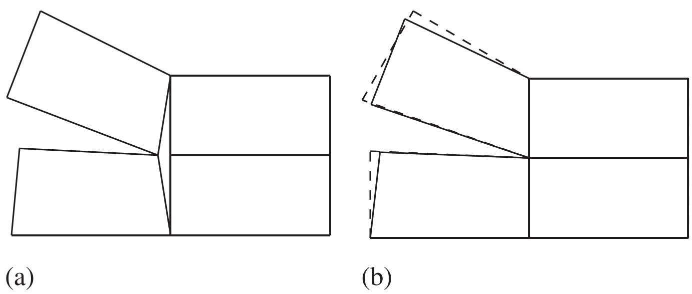

Figure 7. Deformed mesh for soft/stiffer case obtained with: (a) the GSDA; (b) the new formulation (continuous) and GFEM/XFEM (dashed).

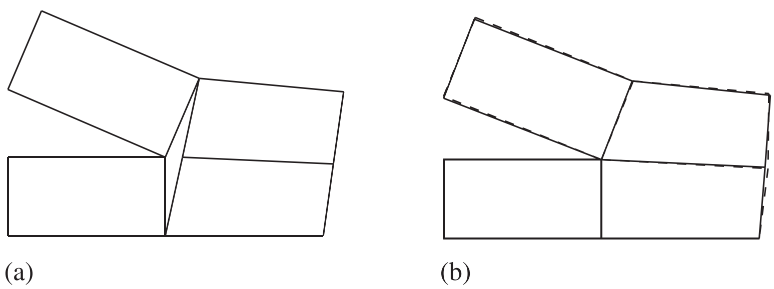

Figure 8. Deformed mesh for stiff/softer case obtained with: (a) the GSDA; (b) the new formulation (continuous) and GFEM/XFEM (dashed).

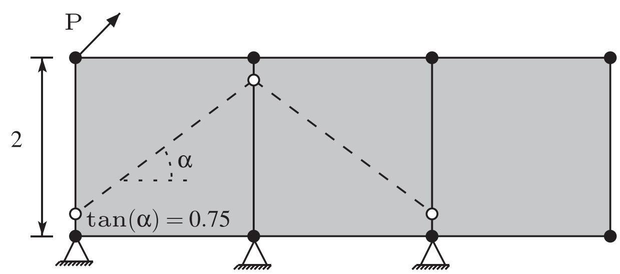

Figure 9. Mesh and loading conditions (dashed line indicates the prescribed discontinuity).

DOI: 10.1002/nme

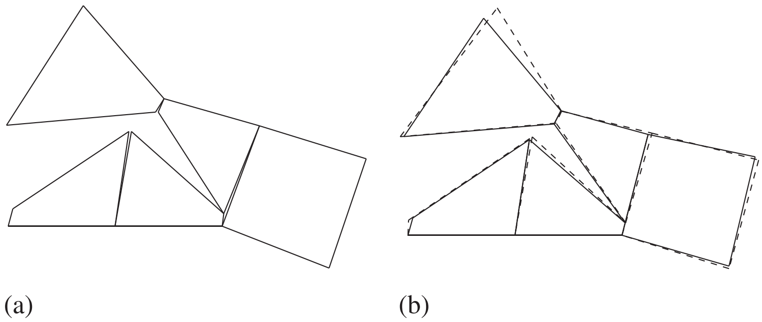

Figure 10. Deformed mesh (displacements magnified 2 times) obtained with (a) the GSDA; and (b) the new formulation (continuous) and GFEM/XFEM (dashed).

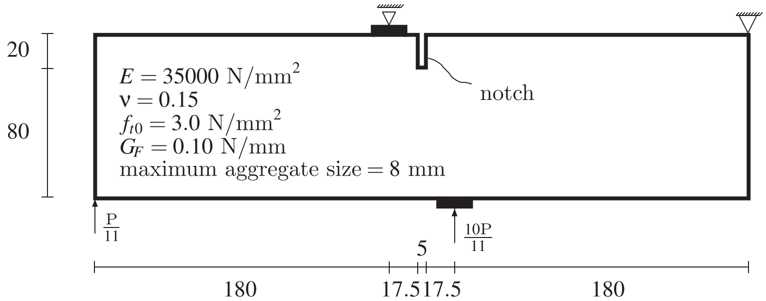

Figure 11. Single-edge notched beam—structural scheme (100 mm width, dimensions in mm).

can be concluded that (i) although with the GSDA both jumps and tractions are continuous across element boundaries, incompatible displacements between elements and at the tip are obtained (Figures 10(a) and 2); (ii) the deformed meshes obtained with the new formulation and GFEM/XFEM are qualitatively better; (iii) the new embedded approach is fully compatible (Figure 10(b)); and (iv) the displacements obtained with both the new formulation and GFEM/XFEM are similar, although the former leads to a slightly stiffer solution than the latter (Figure 10(b)).

5.2. Structural examples

In this section, the following structural examples are presented: (i) a single-edge notched beam [38]; (ii) a double-edge notched specimen subjected to mixed-mode fracture [39]; and (iii) a prenotched gravity dam model [40].

5.2.1. Single-edge notched beam. In this section, a single-edge notched beam of small size composed of normal concrete with maximum aggregate size of 8mm is numerically simulated [38]. The beam measures $400 \times 100 \times 100$ mm^3 and has a $5 \times 20 \times 100$ mm^3 notch located at the top, as shown in Figure 11. The material parameters are as follows: Young's modulus $E = 35\,000$ N/mm^2; Poisson's ratio $\nu = 0.15$; tensile strength $f_{t0} = 3.0$ N/mm^2; and fracture energy $G_F = 0.1$ N/mm. A constitutive law by [41] is adopted with normal stiffness $k_n = 10^5$ N/mm^3 and shear stiffness $k_s = 4 \times 10^2$ N/mm^3.

A mesh composed of 474 bilinear elements is adopted (Figure 12). Loading is controlled using the arc-length method, in which the monotonic increase of the relative sliding displacement of the notch (crack mouth slide displacement, CMSD), is enforced. The discontinuity is constrained to propagate from the notch.

In Figures 13 and 14 the numerical results are presented. In particular, the results obtained with both conforming formulations (the new embedded approach and the GFEM/XFEM) are practically coincident (see CMSD versus load curves in Figure 13(a) and crack path in Figure 13(b)).

DOI: 10.1002/nme

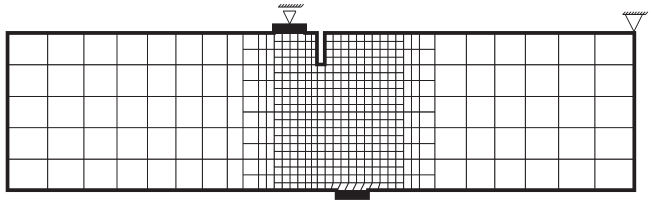

Figure 12. Single edge notched beam – adopted mesh with 474 bilinear finite elements.

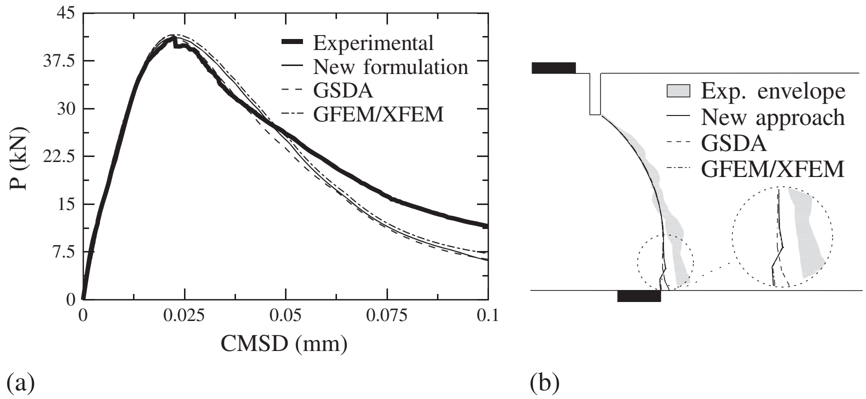

Figure 13. Single-edge notched beam: (a) CMSD versus load curves; and (b) crack path computed at CMSD = 0.1 mm.

In Figure 14(a), non-conforming elements are clearly visible close to the notch, although this is less visible in a later stage (Figure 14(b)).

In this example, the computational time spent on a laptop (i7 M620 2.67 GHz, 8 GB RAM) until CMSD = 0.1 mm is 55 s and 225 steps for all approaches.

5.2.2. Nooru Mohamed's test. This example consists of a double-edge notched specimen subjected to mixed-mode fracture, experimentally tested by [39]. The $200 \times 200 \times 50$ mm^3 specimen has two 25×5 mm^2 horizontal notches located at half height. The specimen is loaded by means of two L-shaped steel frames glued to the specimen. One of the experimental load paths is numerically simulated: (i) a horizontal force P is applied and increased to 10^4 N, after which it is kept constant; and (ii) a vertical displacement u_v is gradually enforced into the top steel frame (Figure 15(a)).

The material parameters are taken from [39]: Poisson's ratio $\nu = 0.2$; Young's modulus $E = 30\,000$ N/mm^2; compressive strength $f_c = 38$ N/mm^2, tensile strength $f_{t0} = 3.0$ N/mm^2; and fracture energy $G_F = 0.11$ N/mm. The initial normal and shear stiffness adopted for the discontinuity is $k_n = k_s = 10^4$ N/mm^3. Upon crack opening, the constitutive law by [31] is adopted, with $\beta = f_{t0}/c_0 = 0.6$, where c_0 is the cohesion estimated using Mohr's rupture theory.

The adopted mesh with 435 bilinear finite elements is represented in Figure 15(b). The arc-length method is used to enforce a monotonic increase in the vertical displacement of the top steel frame (u_v). The discontinuities are inserted from the notch.

All results are shown in Figures 16–18, including the vertical displacement versus load curves, the crack path, the deformed mesh and the map of the first principal stress. It must be stressed that the experimental peak load is smaller than the corresponding numerical values, which is also verified by other authors [42–44].

From the numerical results, it can be observed that, similarly to the previous structural example, the conforming formulations (GFEM/XFEM and the new embedded approach), provide similar displacement versus load curves, crack paths and deformed meshes. Furthermore, the stress map represented in Figure 18 reveals that the new embedded formulation adequately reproduces the stress field in the bulk, with stresses gradually approaching zero in the vicinity of the crack.

DOI: 10.1002/nme

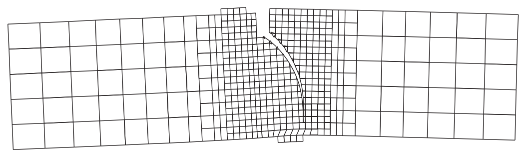

(a)

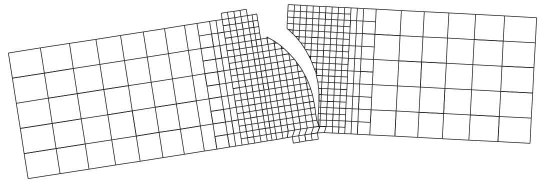

(b)

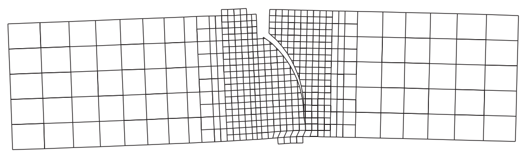

(c)

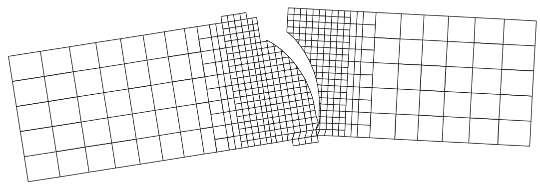

(d)

Figure 14. Single-edge notched beam—deformed mesh (displacements magnified 75 times) obtained with: (a)–(b) the GSDA; and (c)–(d) the new formulation. (a) and (c) correspond to CMSD = 0.05 mm, whereas (b) and (d) correspond to CMSD = 0.1 mm.

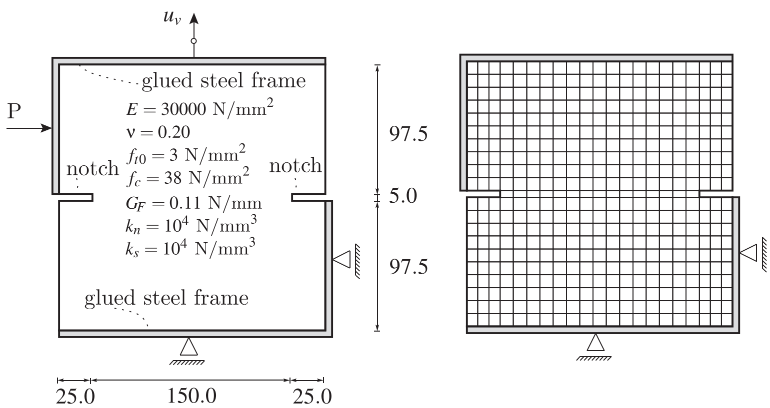

(a) (b)

Figure 15. Nooru Mohamed's test: (a) structural scheme (50 mm width, dimensions in mm); and (b) adopted mesh with 435 bilinear elements.

In this example, the computational time spent on a laptop (i7 M620 2.67 GHz, 8 GB RAM) until $u_v = 0.2$ mm is: 350 s and 152 steps for the new embedded approach; 375 s and 151 steps for the GSDA; and 350 s and 154 steps for the GFEM/XFEM.

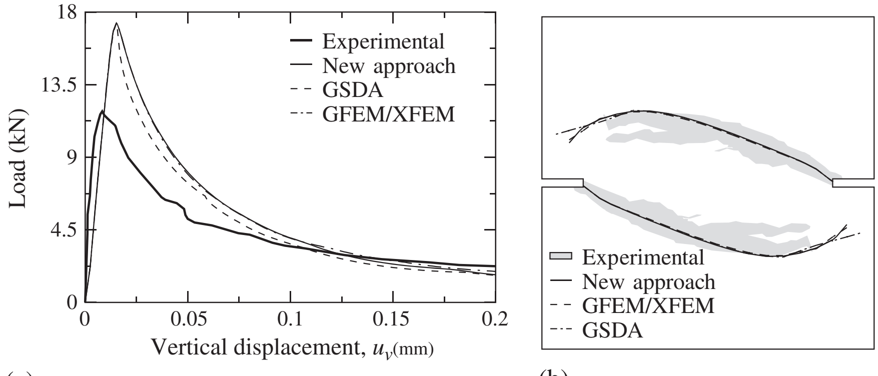

(a) (b)

Figure 16. Nooru Mohamed's test: (a) vertical displacement versus load curves; and (b) crack path computed at $u_v = 0.2$ mm.

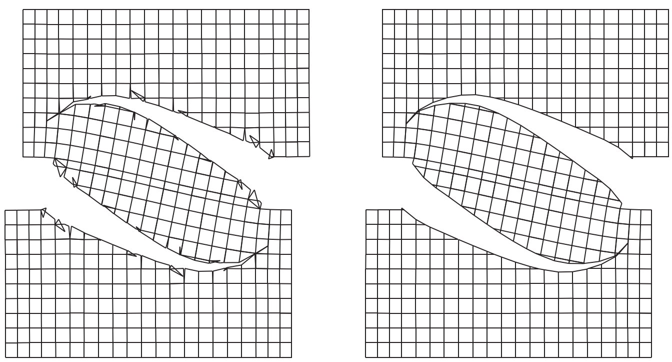

(a) (b)

Figure 17. Nooru Mohamed's test—deformed mesh (displacements magnified 150 times) for $u_v = 0.2$ mm obtained with: (a) the GSDA; and (b) the new formulation.

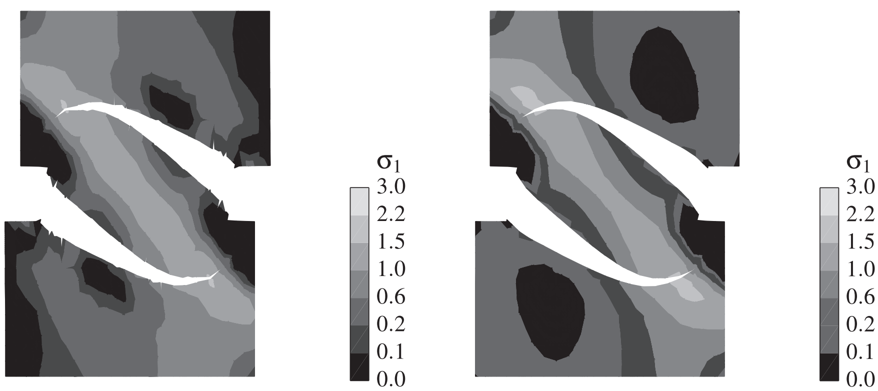

(a) (b)

Figure 18. Nooru Mohamed's test - principal stress σ_1 (displacements magnified 150 times) for $u_v = 0.2$ mm obtained with: (a) the GSDA; and (b) the new formulation.

5.2.3. Prenotched gravity dam model. An experimental test performed by [40] on a dam is numerically simulated in this section. The corresponding structural scheme is represented in Figure 19.

The material parameters are adopted from [40]: Young's modulus $E = 35\,700$ N/mm^2; Poisson's ratio $\nu = 0.1$; dead weight $\rho = 2400$ kg/m^3; tensile strength $f_{t0} = 3.6$ N/mm^2; and fracture energy $G_F = 0.184$ N/mm. Additionally, an exponential softening law is adopted for the constitutive relation between the normal component for mode-I opening, whereas the shear stiffness is assumed to gradually drop towards zero, proportionally to the mode-I secant stiffness.

The mesh is composed of 1848 bilinear finite elements (Figure 20). A refinement is performed near the notch to better evaluate the stress at the discontinuity. Non-proportional loading is applied: first, the dead load is introduced; afterwards, the water pressure in front of the dam is gradually increased. In both cases, the arc-length method is used to enforce an increase of the relative crack mouth opening displacement (CMOD).

The load versus CMOD curves are presented in Figure 21. It can be observed that the numerical results are similar to the experimental results from [40]. Furthermore, it is again confirmed that the conforming formulations lead to almost coincident results with GFEM/XFEM.

A good agreement between the numerical and the experimental crack path is found, as represented in Figure 22. Some differences between formulations only appear in the later stages of propagation, where the coarser mesh is clearly insufficient for the evaluation of the crack path.

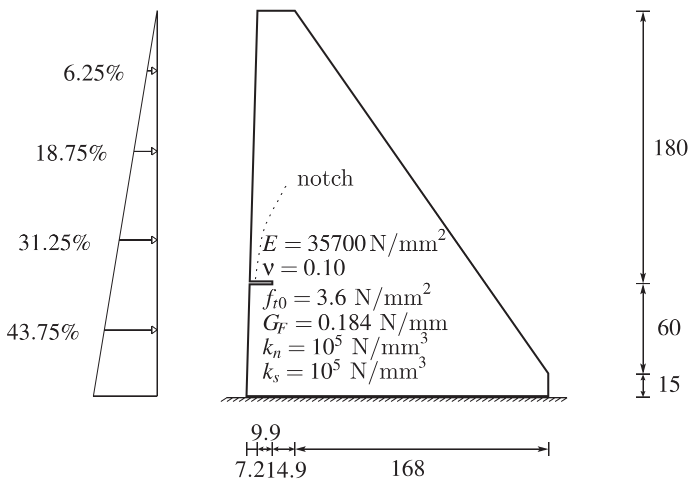

Figure 19. Prenotched gravity dam model—structural scheme (30cm width, dimensions in cm).

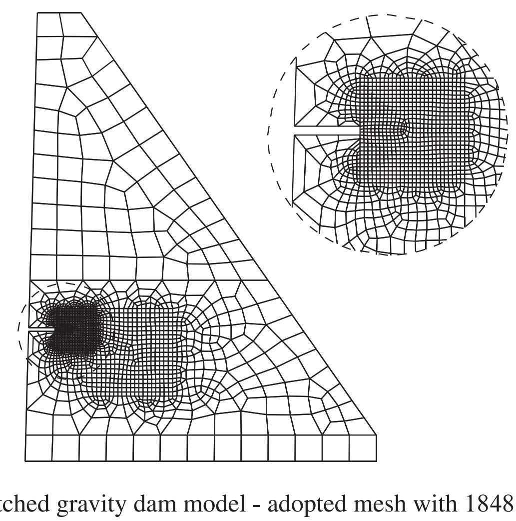

Figure 20. Prenotched gravity dam model - adopted mesh with 1848 bilinear elements.

DOI: 10.1002/nme

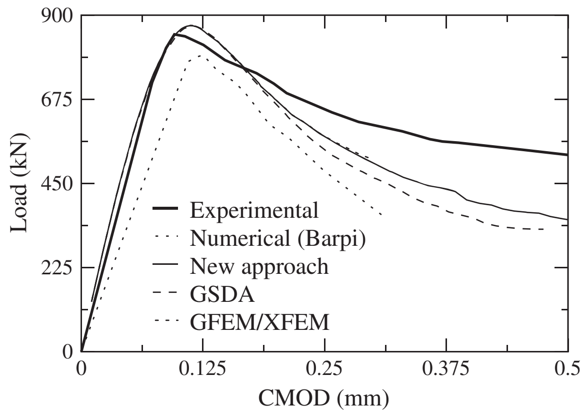

Figure 21. Prenotched gravity dam model—load versus CMOD curves superposed with experimental and numerical results from [40].

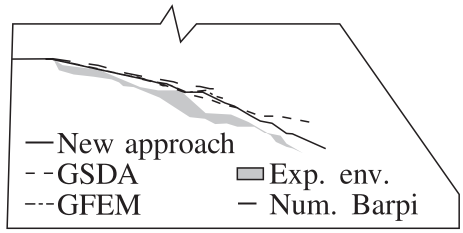

Figure 22. Prenotched gravity dam model—crack path, obtained when CMOD is 0.50 mm, superposed with experimental and numerical results from [40].

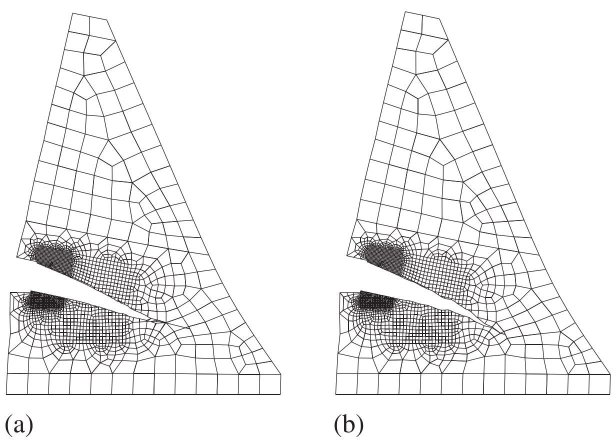

Figure 23. Prenotched gravity dam model—deformed mesh (displacements amplified 500 times) for CMOD 0.50 mm obtained with: (a) the GSDA; and (b) the new formulation.

The deformed mesh is represented in Figure 23, when the CMOD is 0.5 mm, for the GSDA and the new embedded approach. Additionally, in Figure 24, the σ_1 stress map is also represented.

In this example, the computational time spent on a laptop (i7 M620 2.67 GHz, 8 GB RAM) until CMOD 0.50 mm is: 340 s and 86 steps for the new embedded approach; 345 s and 81 steps for the GSDA; and 395 s and 83 steps for the GFEM/XFEM. This is the only example where the computing time has been slightly larger with GFEM/XFEM due to the significant increase in the required number of DOFs.

DOI: 10.1002/nme

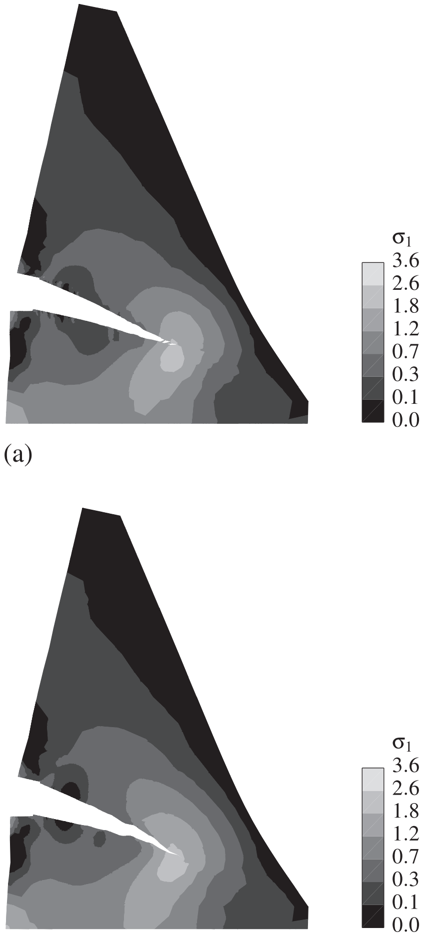

(a)

(b)

Figure 24. Prenotched gravity dam model—principal stress σ_1 (displacements amplified 500 times) for CMOD 0.50 mm obtained with (a) the GSDA; and (b) the new formulation.

6. CONCLUSIONS

A new formulation using conforming finite elements with embedded strong discontinuities was presented. Compared with previous embedded approaches, namely [11, 12, 18–21, 45, 46]: (i) no additional DOFs are required; and (ii) the continuity of both tractions and enhanced kinematical field across elements is automatically ensured. The proposed formulation is variationally consistent and built upon the framework of the discrete crack approach. Therefore, mesh objectivity is automatically inherited.

The presented structural examples allowed to conclude that the new embedded formulation is capable of providing results, which are practically indistinguishable from the results obtained with GFEM/XFEM.

However, in spite of the common variational framework [32] and similar results, the two formulations are built in a significantly different manner. The following main differences can be advanced:

- the GFEM/XFEM is nodal based whereas the present formulation is built at element level;
- crack propagation is simpler to implement in the embedded approach as only crossed finite elements are enriched, instead of all nodes surrounding the discontinuity, as typically performed in GFEM/XFEM;

- with the embedded formulation, only one additional node is required at each new enriched finite element because of crack propagation, whereas with GFEM/XFEM, all nodes supporting the discontinuity must be enriched;
- with the present formulation, all additional DOFs are located at the discontinuity, where the quantities of interest are measured.

Finally, although the observed computational cost was similar for the bi-dimensional structural problems earlier presented, the embedded formulation is expected to gain advantage in three-dimensional problems because significantly fewer DOFs are required for each enriched finite element.

ACKNOWLEDGEMENTS

This work is supported by FEDER funds through the Operational Programme for Competitiveness Factors - COMPETE - and by Portuguese funds through FCT - Portuguese Foundation for Science and Technology under Project No. FCOMP-01-0124-FEDER-020275 (FCT ref. PTDC/ECM/119214/2010).

REFERENCES

1. Reyes E, Casati MJ, Gálvez JC. Cohesive crack model for mixed mode fracture of brick masonry. *International Journal of Fracture* 2008; **151**(1):29–55. DOI: 10.1007/s10704-008-9243-1.
2. Reyes E, Gálvez JC, Casati MJ, Cendón DA, Sancho JM, Planas J. An embedded cohesive crack model for finite element analysis of brickwork masonry fracture. *Engineering Fracture Mechanics* 2009; **76**(12):1930–1944. DOI: 10.1016/j.engfrac mech.2009.05.002.
3. Armero F, Linder C. Numerical simulation of dynamic fracture using finite elements with embedded discontinuities. *International Journal of Fracture* 2009; **160**(2):119–141. DOI: 10.1007/s10704-009-9413-9.
4. Armero F, Garikipati K. An analysis of strong discontinuities in multiplicative finite strain plasticity and their relation with the numerical simulation of strain localization in solids. *International Journal of Solids and Structures* 1996; **33**(20-22):2863–2885. DOI: 10.1016/0020-7683(95)00257-X.
5. Armero F, Linder C. New finite elements with embedded strong discontinuities in the finite deformation range. *Computer Methods in Applied Mechanics and Engineering* 2008; **197**(33-40):3138–3170. DOI: 10.1016/j.cma.2008.02.021.
6. Graça-e-Costa R, Alfaiate J. The numerical analysis of reinforced concrete beams using embedded discontinuities. *Structural Durability & Health Monitoring* 2006; **2**(1):11–18.
7. Oliver J, Linero DL, Huespe AE, Manzoli OL. Two-dimensional modeling of material failure in reinforced concrete by means of a continuum strong discontinuity approach. *Computer Methods in Applied Mechanics and Engineering* 2008; **197**(5):332–348. DOI: 10.1016/j.cma.2007.05.017.
8. Simo JC, Rifai MS. A class of mixed assumed strain methods and the method of incompatible modes. *International Journal for Numerical Methods in Engineering* 1990; **29**(8):1595–1638. DOI: 10.1002/nme.1620290802.
9. Simo JC, Oliver J, Armero F. An analysis of strong discontinuities induced by strain-softening in rate-independent inelastic solids. *Computational Mechanics* 1993; **12**(5):277–296. DOI: 10.1007/BF00372173.
10. Larsson R, Runesson K. Element-embedded localization band based on regularized displacement discontinuity. *Journal of Engineering Mechanics* 1996; **122**(5):402–411. DOI: 10.1061/(AS CE)0733-9399(1996)122:5(402).
11. Oliver J. Modelling strong discontinuities in solid mechanics via strain softening constitutive equations. Part 1: fundamentals. *International Journal for Numerical Methods in Engineering* 1996; **39**(21):3575–3600.
12. Oliver J. Modelling strong discontinuities in solid mechanics via strain softening constitutive equations. Part 2: numerical simulation. *International Journal for Numerical Methods in Engineering* 1996; **39**(21):3601–3623. DOI: 10.1002/(SICI)1097-0207(19961115)39:21<3601::AID-NME64>3.0.CO;2 -4.
13. Ohlsson U, Olofsson T. Mixed-mode fracture and anchor bolts in concrete analysis with inner softening bands. *Journal of Engineering Mechanics* 1997; **123**(10):1027–1033. DOI: 10.1061/(ASCE)0733-9399(1997)123:10(1027).
14. Jirásek M, Zimmermann T. Embedded crack model: Part I. Basic formulation. *International Journal for Numerical Methods in Engineering* 2001; **50**(6):1269–1290.
15. Jirásek M, Zimmermann T. Embedded crack model: Part II. Combination with smeared cracks. *International Journal for Numerical Methods in Engineering* 2001; **50**(6):1291–1305.
16. Borja RI. A finite element model for strain localization analysis of strongly discontinuous fields based on standard Galerkin approximation. *Computer Methods in Applied Mechanics and Engineering* 2000; **190**:1529–1549. DOI: 10.1016/S0045-7825(00)00176-6.
17. Bolzon G. Formulation of a triangular finite element with an embedded interface via isoparametric mapping. *Computational Mechanics* 2001; **27**(6):463–473. DOI: 10.1007/s004660100257.
18. Alfaiate J, Simone A, Sluys LJ. Non-homogeneous displacement jumps in strong embedded discontinuities. *International Journal of Solids and Structures* 2003; **40**(21):5799–5817. DOI: 10.1016/S0020-7683(03)00372-X.
19. Dias-da-Costa D, Alfaiate J, Sluys LJ, Júlio ENBS. A discrete strong discontinuity approach. *Engineering Fracture Mechanics* 2009; **76**(9):1176–1201. DOI: 10.1016/j.engfrac mech.2009.01.011.

20. Linder C, Armero F. Finite elements with embedded strong discontinuities for the modeling of failure in solids. *International Journal for Numerical Methods in Engineering* 2007; **72**(12):1391–1433. DOI: 10.1002/nme.2042.
21. Dias-da-Costa D, Alfaiate J, Sluys LJ, Júlio ENBS. Towards a generalization of a discrete strong discontinuity approach. *Computer Methods in Applied Mechanics and Engineering* 2009; **198**(47-48):3670–3681. DOI: 10.1016/j.cma.2009.07.013.
22. Duarte CAM, Oden JT. Hp clouds—a meshless method to solve boundary-value problems. *Technical Report 95-05*, TICAM, University of Texas at Austin, 1995.
23. Belytschko T, Black T. Elastic crack growth in finite elements with minimal remeshing. *International Journal for Numerical Methods in Engineering* 1999; **45**(5):601–620.
24. Simone A. Partition of unity-based discontinuous elements for interface phenomena: computational issues. *Communications in Numerical Methods in Engineering* 2004; **20**(6):465–478. DOI: 10.1002/cnm.688.
25. Wells GN, Sluys LJ. A new method for modelling cohesive cracks using finite elements. *International Journal for Numerical Methods in Engineering* 2001; **50**(12):2667–2682. DOI: 10.1002/nme.143.
26. Alfaiate J, Sluys LJ. On the use of embedded discontinuities in the framework of a discrete crack approach. In *WCCM VI*. Tsinghua University Press & Springer-Verlag: Beijing, China, 2004.
27. Klisinski M, Runesson K, Sture S. Finite element with inner softening band. *Journal of Engineering Mechanics* 1991; **117**(3):575–587. DOI: 10.1061/(AS CE)0733-9399(1991)117:3(575).
28. Lofti HR, Shing PB. Embedded representation of fracture in concrete with mixed finite elements. *International Journal for Numerical Methods in Engineering* 1995; **38**(8):1307–1325. DOI: 10.1002/nme.1620380805.
29. Remmers JJC. Discontinuities in materials and structures: a unifying computational approach. *PhD Thesis*, Delft University of Technology, 2006.
30. Malvern LE. *Introduction to the Mechanics of a Continuous Medium*. Prentice-Hall International: Englewood Cliffs, New Jersey, 1969.
31. Alfaiate J, Wells GN, Sluys LJ. On the use of embedded discontinuity elements with crack path continuity for mode-I and mixed-mode fracture. *Engineering Fracture Mechanics* 2002; **69**(6):661–686. DOI: 10.1016/S0013-7944(01)00108-4.
32. Dias-da-Costa D, Alfaiate J, Sluys LJ, Júlio ENBS. A comparative study on the modelling of discontinuous fracture by means of enriched nodal and element techniques and interface elements. *International Journal of Fracture* 2010; **161**(1):97–119. DOI: 10.1007/s10704-009-9432-6.
33. Carol I, Prat PC. A multicrack model based on the theory of multisurface plasticity and two fracture energies. In *COMPLAS IV - Computational Plasticity, Fundamentals and Applications*, Owen DRJ, Oñate E, Hinton E (eds). Pineridge Press: Barcelona, Spain, 1995; 1583–1594.
34. Carol I, Prat PC, Lopez CM. Normal/shear cracking model: application to discrete crack analysis. *Journal of Engineering Mechanics* 1997; **123**(8):765–773.
35. Lourenço PB, Rots JG. Multisurface interface model for analysis of masonry structures. *Journal of Engineering Mechanics* 1997; **123**(7):660. DOI: 10.1061/(AS CE)0733-9399(1997)123:7(660).
36. Alfaiate J, Almeida JR. Modelling discrete cracking on masonry walls. *Masonry International* 2004; **17**(2):83–93.
37. Hillerborg A, Modeer M, Petersson PE. Analysis of crack formation and crack growth in concrete by means of fracture mechanics and finite elements. *Cement and Concrete Research* 1976; **6**(6):773–781. DOI: 10.1016/0008-8846(76)90007-7.
38. Schlangen E. Experimental and numerical analysis of fracture processes in concrete. *PhD Thesis*, Delft University of Technology, 1993.
39. Nooru-Mohamed MB. Mixed-mode fracture of concrete: an experimental approach. *PhD Thesis*, Delft University of Technology, 1992.
40. Barpi F, Valente S. Numerical simulation of prenotched gravity dam models. *Journal of Engineering Mechanics* 2000; **126**(6):611–619. DOI: 10.1061/(AS CE)0733-9399(2000)126:6(611).
41. Wells GN, Sluys LJ. Three-dimensional embedded discontinuity model for brittle fracture. *International Journal of Solids and Structures* 2001; **38**(5):897–913. DOI: 10.1016/S0020-7683(00)00029-9.
42. Pivonka P, Ozbolt J, Lackner R, Mang HA. Comparative studies of 3D-constitutive models for concrete: application to mixed-mode fracture. *International Journal for Numerical Methods in Engineering* 2004; **60**(2):549–570. DOI: 10.1002/nme.975.
43. Cervera M, Chiumenti M. Smeared crack approach: back to the original track. *International Journal for Numerical and Analytical Methods in Geomechanics* 2006; **30**(12):1173–1199. DOI: 10.1002/nag.518.
44. Gasser TC, Holzapfel GA. 3D crack propagation in unreinforced concrete: a two-step algorithm for tracking 3D crack paths. *Computer Methods in Applied Mechanics and Engineering* 2006; **195**(37-40):5198–5219. DOI: 10.1016/j.cma.2005.10.023.
45. Oliver J, Cervera M, Manzoli O. Strong discontinuities and continuum plasticity models: the strong discontinuity approach. *International Journal of Plasticity* 1999; **15**(3):319–351. DOI: 10.1016/S0749-6419(98)00073-4.
46. Oliver J. Contributions to the continuum modelling of strong discontinuities in two-dimensional solids. *Tech Report*, Centro Internacional de Métodos Numéricos en Ingeniería, 2003.